Supplementary Material

MOF-derived CeO_2 Catalysts with Pr Doping: Engineering Oxygen Vacancies for Improved CO_2 conversion to Dimethyl Carbonate

Jungseob So[a,1], Min Hye Jeong[b,1], Jungwon Yun[c,1], Byeong-Seon An[d], Seung-ik Kim[a], Geun-yeong Kim[a] Hyun-Tak Kim[a], Tae Sun Chang[a], Jin Hee Lee[a], Iljeong Heo[a], Jinjoo An[e], Young Woo You[a,*], Minkyu Kim[f,*], Young Jin Kim[g,*]

[a]*CO_2 & Energy Research Center, Korea Research Institute of Chemical Technology (KRICT), Daejeon 34141, Republic of Korea*

[b]*Clean Air Research Laboratory, Korea Institute of Energy Research (KIER), 152 Gajeong-ro, Daejeon 34129, Republic of Korea*

[c]*William G. Lowrie Chemical & Biomolecular Engineering, The Ohio State University, Ohio 43210, United States*

[d]*Analysis Center for Energy Research, Korea Institute of Energy Research (KIER), 152 Gajeong-ro, Daejeon 34129, Republic of Korea*

[e]*Chemical Process Solution Research Center, Korea Research Institute of Chemical Technology (KRICT), Daejeon 34141, Republic of Korea*

[f]*School of Chemical Engineering, Yeungnam University, 280 Daehak-ro, Gyeongsan 38541, Republic of Korea*

[g]*Department of Environmental Engineering, Kyungpook National University, 80 Daehak-ro, Daegu 41566, Republic of Korea*

[1] These authors contributed equally to this work.

∗ Corresponding author.
E-mail address: ywyou@krict.re.kr (Y.W. You), mk_kim@ynu.ac.kr (M. Kim), yjkim03@knu.ac.kr (Y.J. Kim)

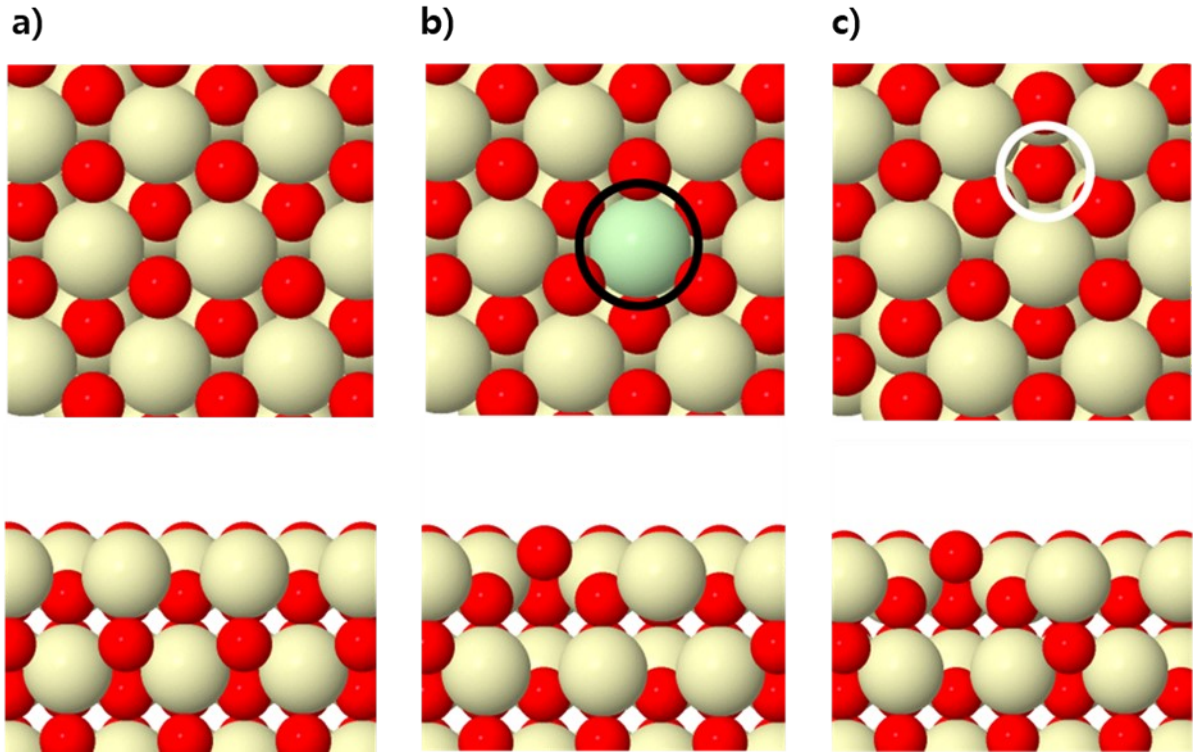

Fig. S1. Top and side views of the **a)** Pristine CeO_2 (111), **b)** Pr substituted CeO_2 (111) (Pr atom indicated with black solid line), and **c)** CeO_2 (111) with 1 O_V surfaces (O_V indicated with white solid line).

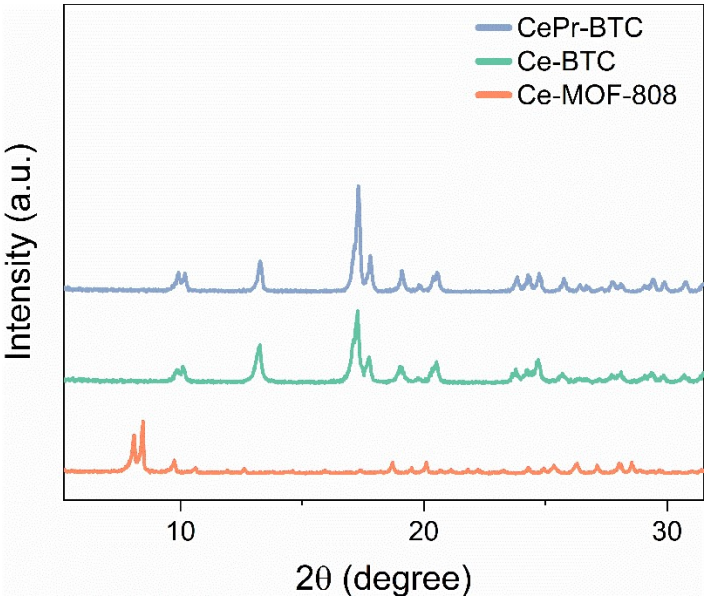

Fig. S2. X-ray diffraction (XRD) patterns of a series of sacrificial Ce-MOF templates.

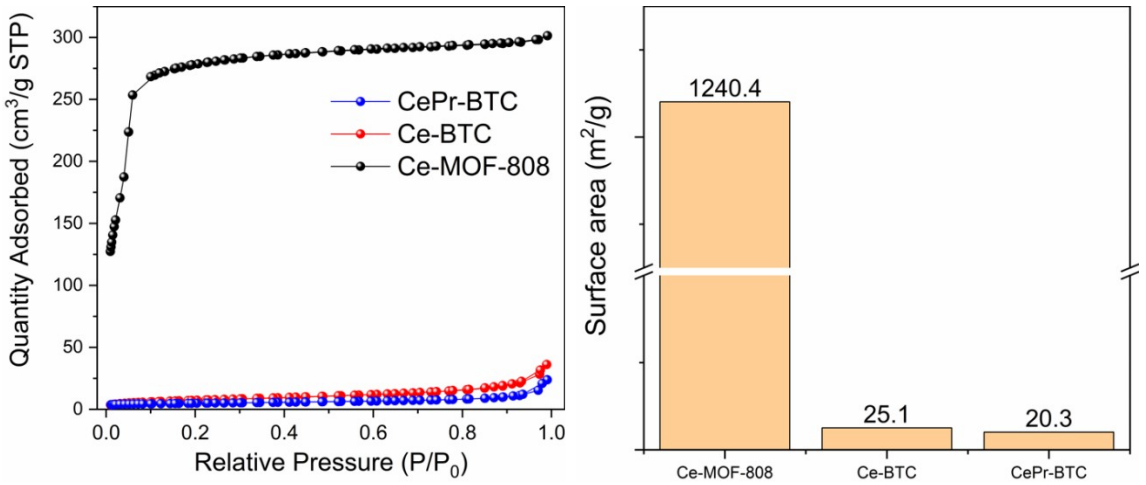

Fig. S3. Nitrogen adsorption-desorption isotherms and the corresponding BET surface area of a series of sacrificial Ce-MOF templates.

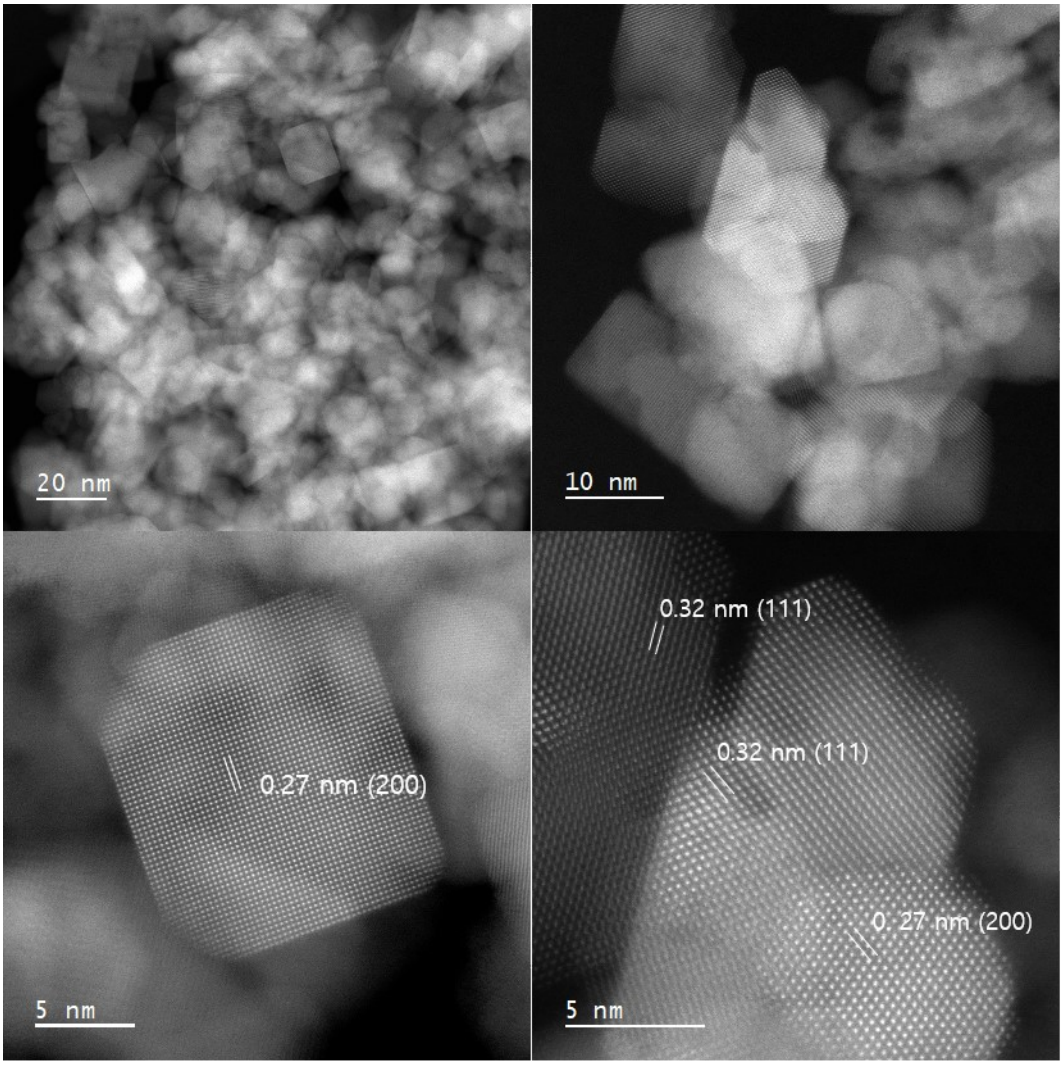

Fig. S4. HAADF-HRSTEM images of CeO_2 (P).

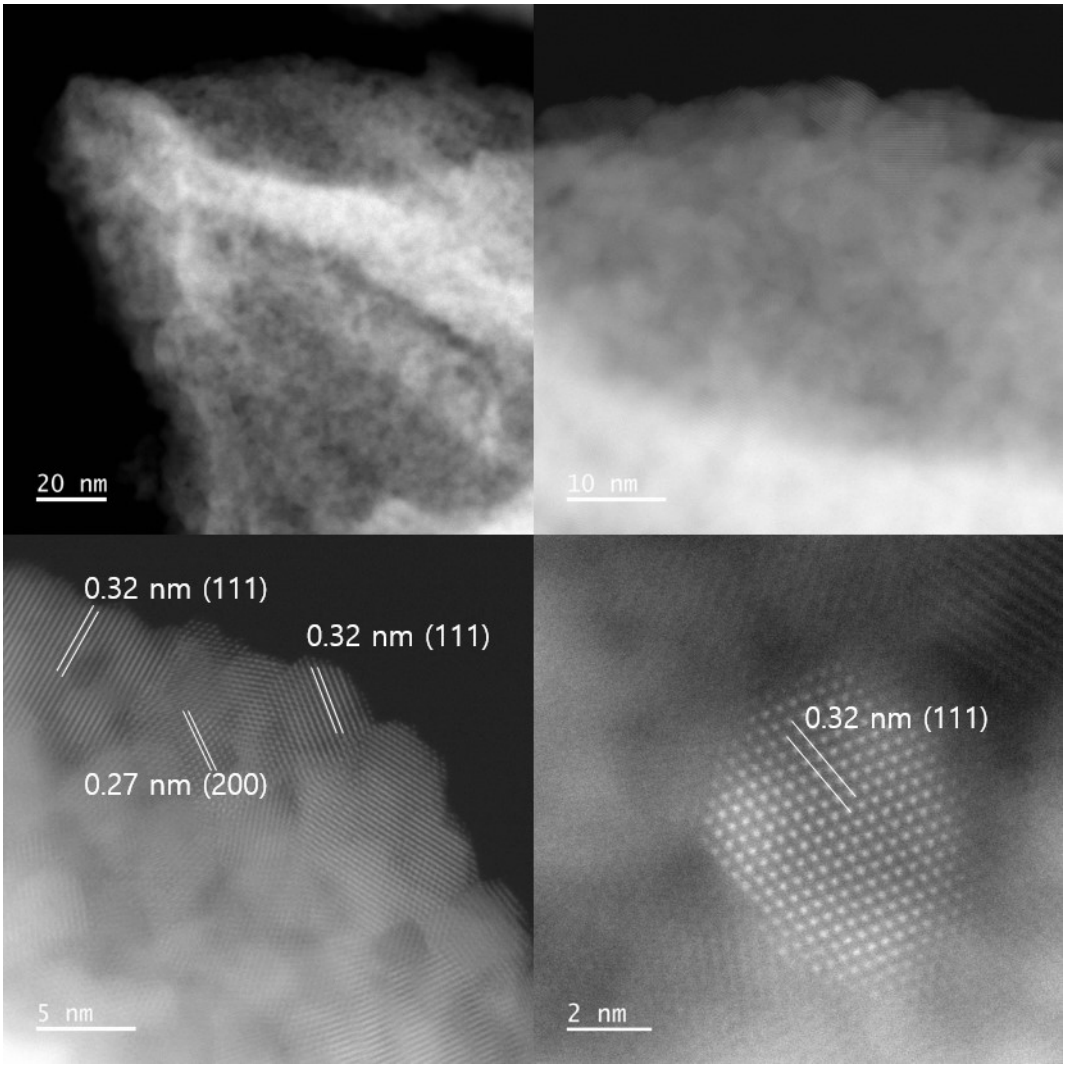

Fig. S5. HAADF-HRSTEM images of CeO_2 (808).

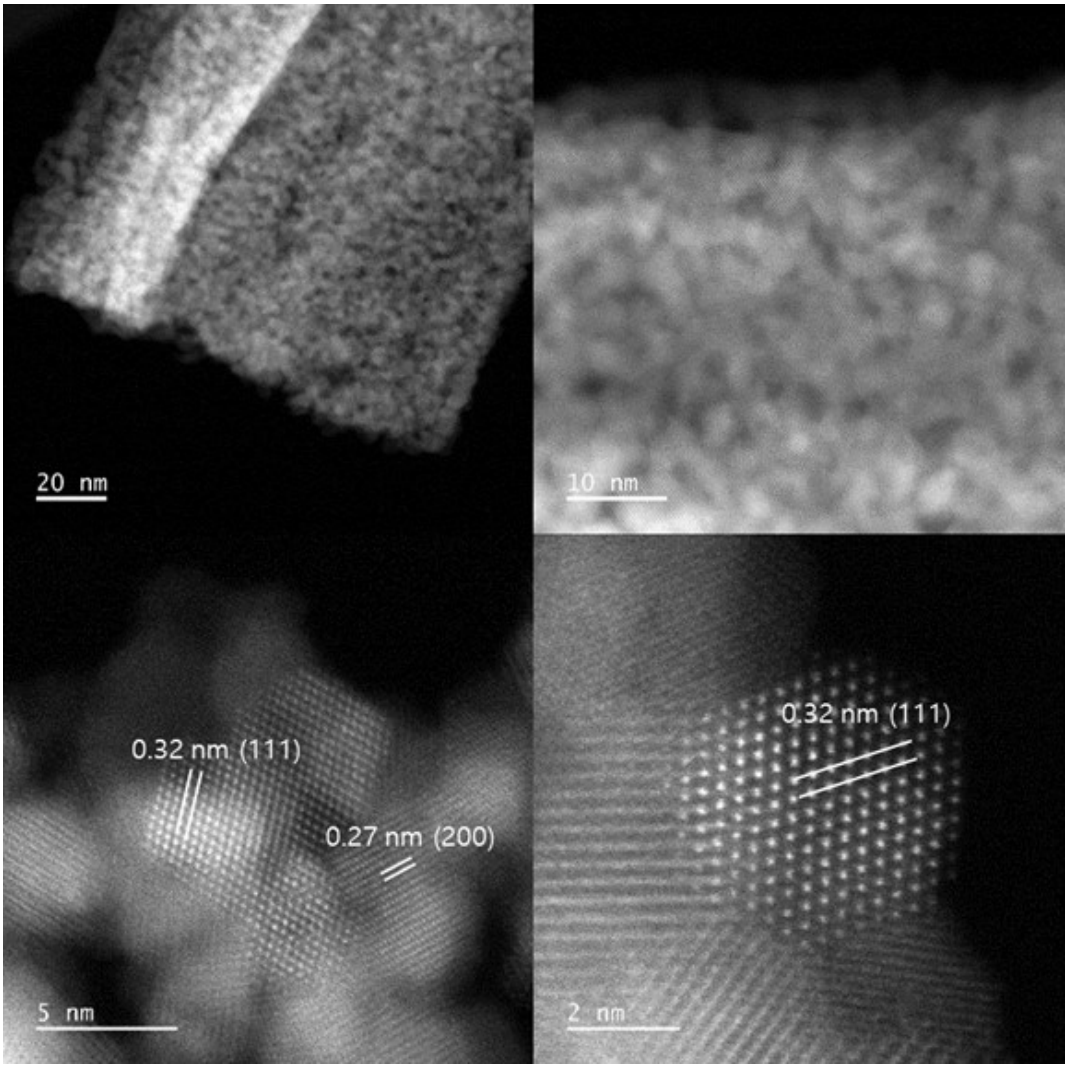

Fig. S6. HAADF-HRSTEM images of CeO_2 (BTC).

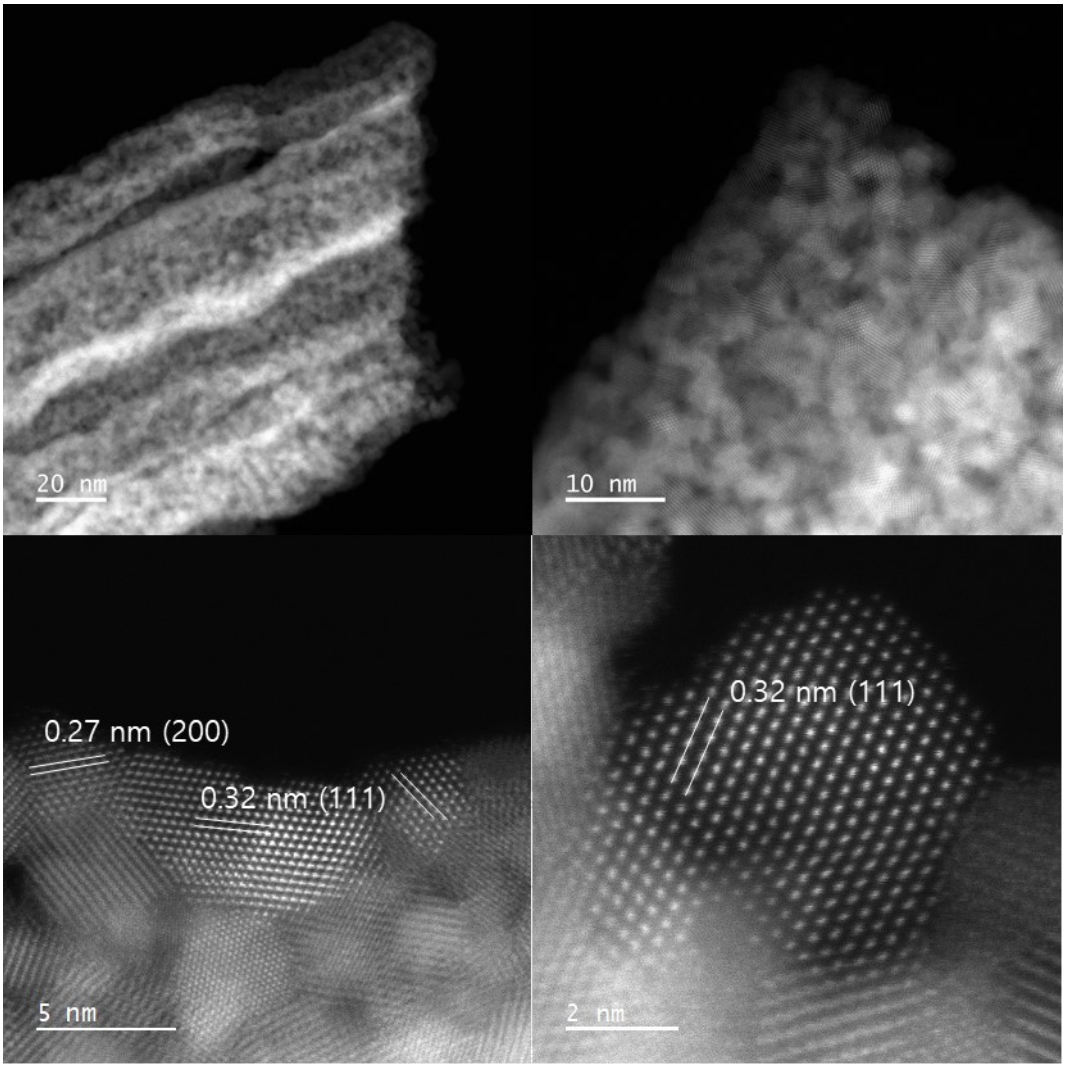

Fig. S7. HAADF-HRSTEM images of CePrOx (BTC).

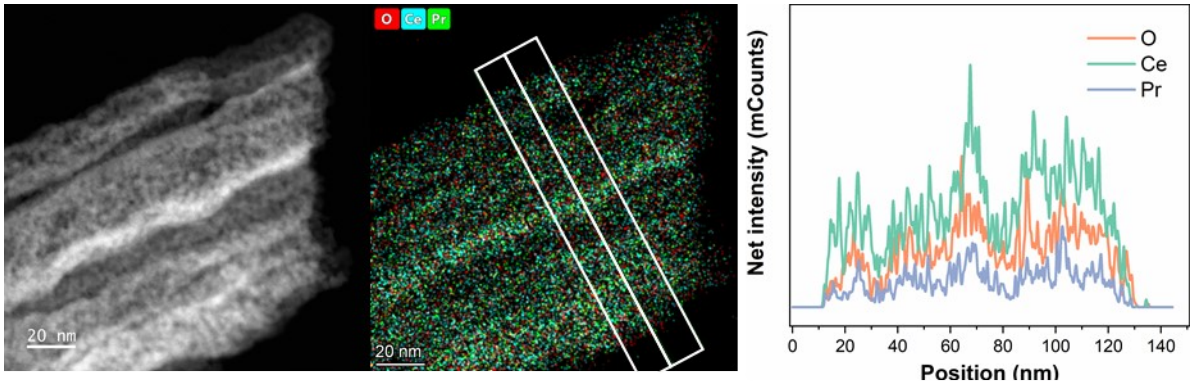

Fig. S8. HAADF-STEM image, the EDX, and the corresponding line profile analysis of CePrOx (BTC).

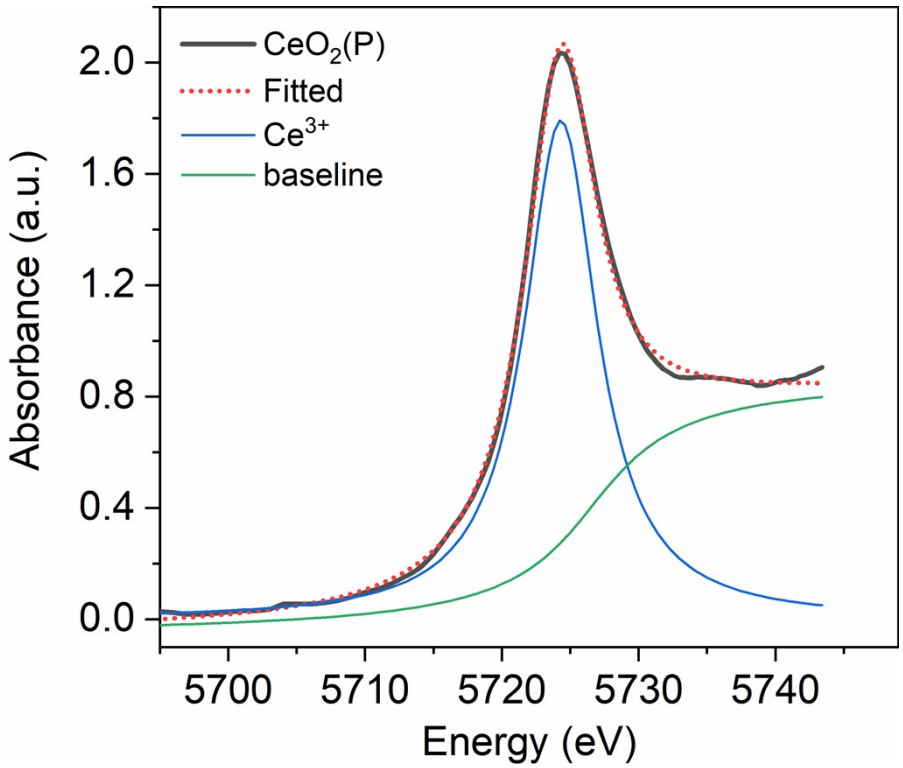

Fig. S9. Ce L_{III} edge XANES spectra of cerium nitrate (Ce^{3+}).

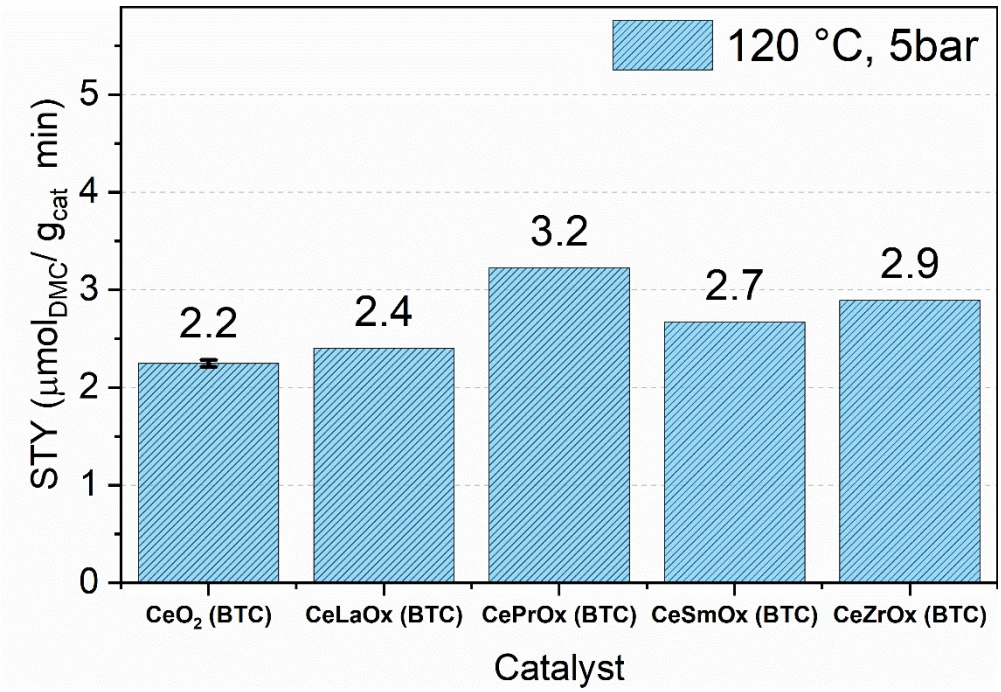

Fig. S10. The effect of doping materials on the catalytic performance of MOF-derived ceria in the DMC synthesis from CO_2 and MeOH at 5 bars. Conditions: a methanol flow rate of 18 µl/min and a CO_2 flow rate of 50 sccm, with performance measurements taken 100 minutes after initiating the reaction.

.

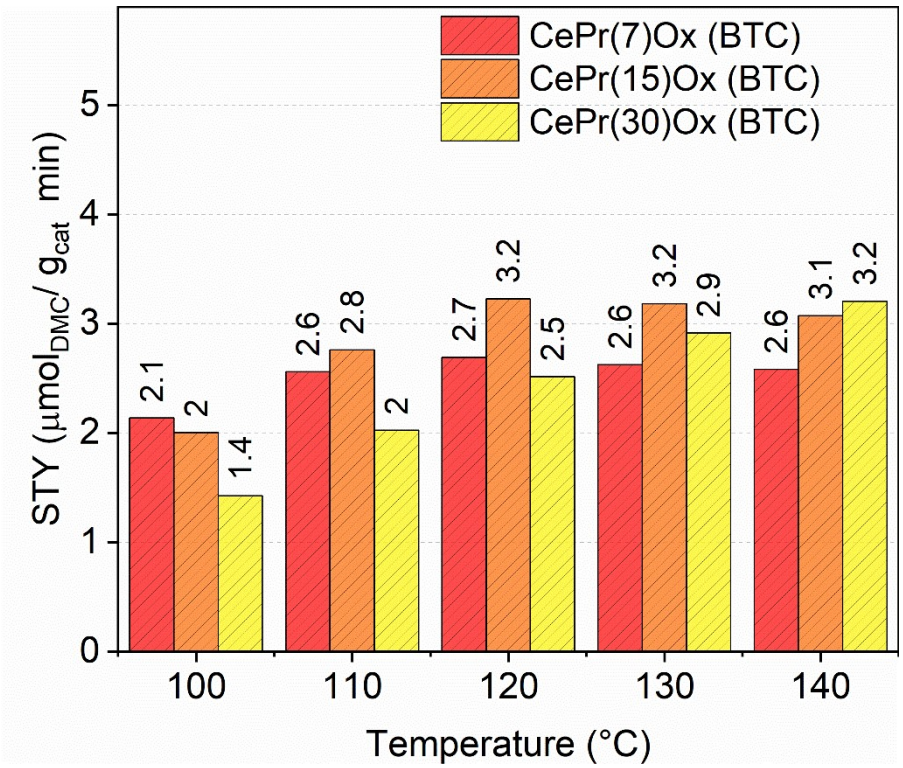

Fig. S11. The effect of Pr content on the catalytic performance of CePr(x)Ox (BTC) samples (x = weight percentage of Pr in the mixed oxides) in the DMC synthesis from CO_2 and MeOH at 5 bars. Conditions: a methanol flow rate of 18 μl/min and a CO_2 flow rate of 50 sccm, with performance measurements taken 100 minutes after initiating the reaction.

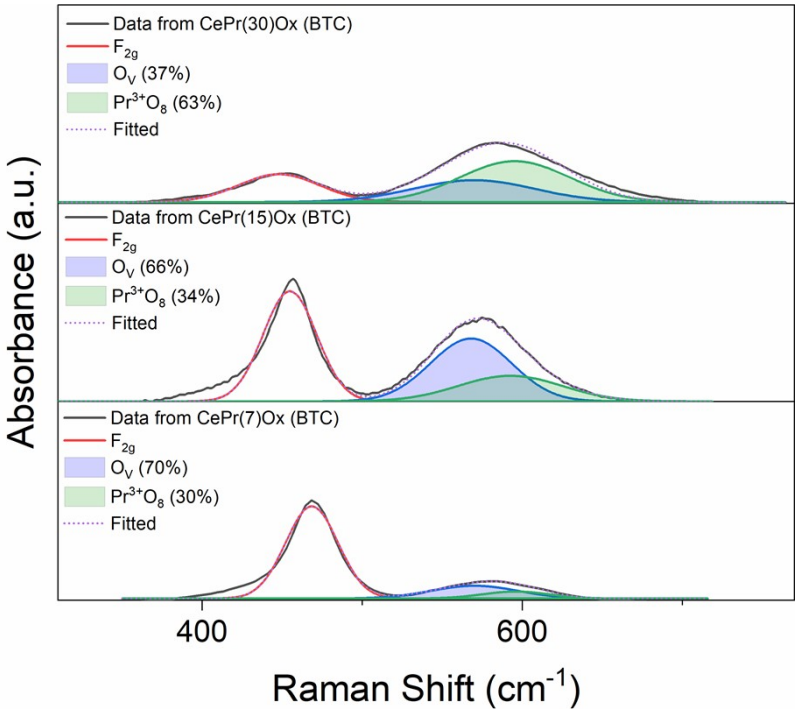

Fig. S12. Raman spectra of CePr(x)Ox (BTC) (x = weight percentage of Pr in the mixed oxides) samples with fitted curves.

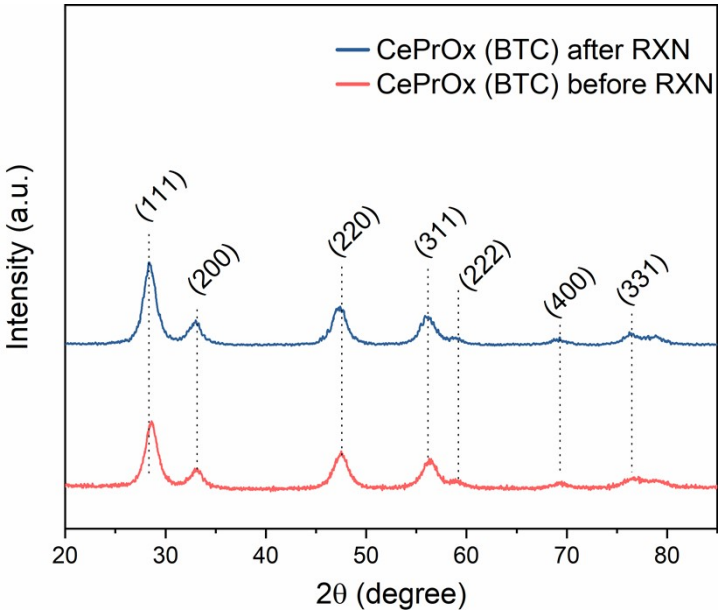

Fig. S13. X-ray diffraction (XRD) patterns of CePrOx (BTC) before and after the reaction. Reaction conditions: methanol flow rate of 18 μL/min and CO_2 flow rate of 50 sccm, conducted at 10 bar and 120 °C.

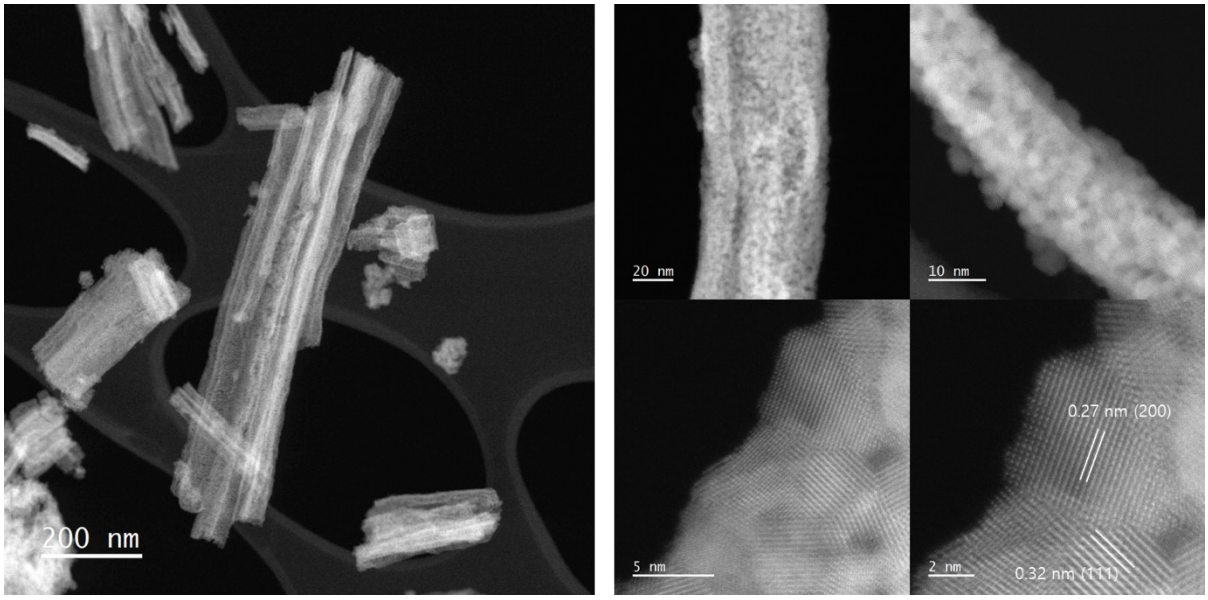

Fig. S14. HAADF-STEM images of CePrOx (BTC) after reaction. Reaction conditions: methanol flow rate of 18 μL/min and CO_2 flow rate of 50 sccm, conducted at 10 bar and 120 °C.

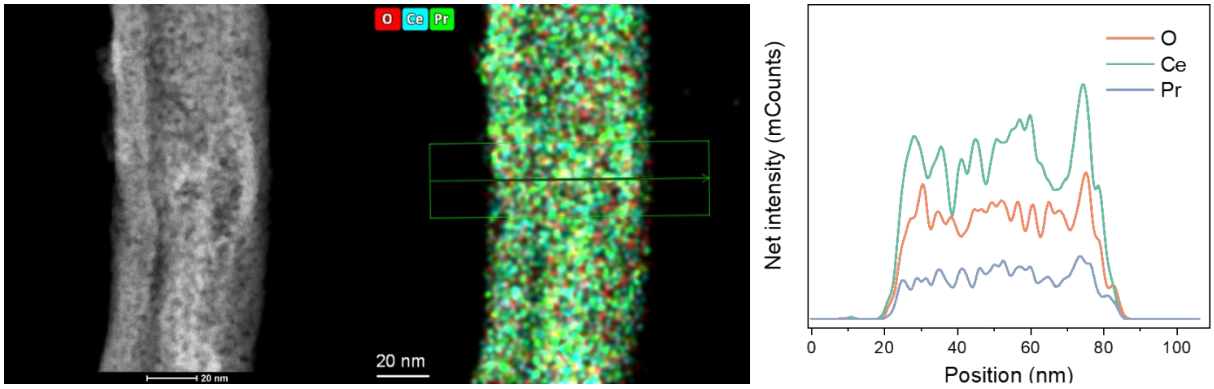

Fig. S15. HAADF-STEM image, the EDX, and the corresponding line profile analysis of CePrOx (BTC) after reaction. Reaction conditions: methanol flow rate of 18 µL/min and CO_2 flow rate of 50 sccm, conducted at 10 bar and 120 °C.

Favored Configurations of CO_2, CH_3OH and DMC on CeO_2(111)

We investigate the favored configurations with corresponding adsorption energies of CO_2, CH_3OH and $CH_3OCOOCH_3$ (DMC) on pristine CeO_2(111), Pr-substituted CeO_2 (111), O_v-CeO_2 (111) and Pr&Ov CeO_2 (111) surfaces shown in the figure S9-11. The adsorption energy of CO_2 exhibits similar values across all surfaces, with the strongest adsorption observed on the O_v-CeO_2 (111) surface (~ 38.7 kJ/mol) and the weakest on the Pr-substituted CeO_2 (111) surface (~ 29.2 kJ/mol). For CH_3OH, we observe relatively weak adsorption on both the pristine and Pr-substituted CeO_2 (111) surfaces, with binding energies of approximately 69 kJ/mol, whereas stronger adsorption is observed on surfaces containing oxygen vacancies (O_V-CeO_2 (111) and Pr&O_V-CeO_2 (111)), with binding energies of approximately 99 kJ/mol. Upon formation of DMC, a similar trend is observed to that of CH_3OH, with relatively weak binding energies observed on both the pristine and Pr-substituted surfaces, and strong binding energies observed on Pr&O_V-CeO_2 (111).

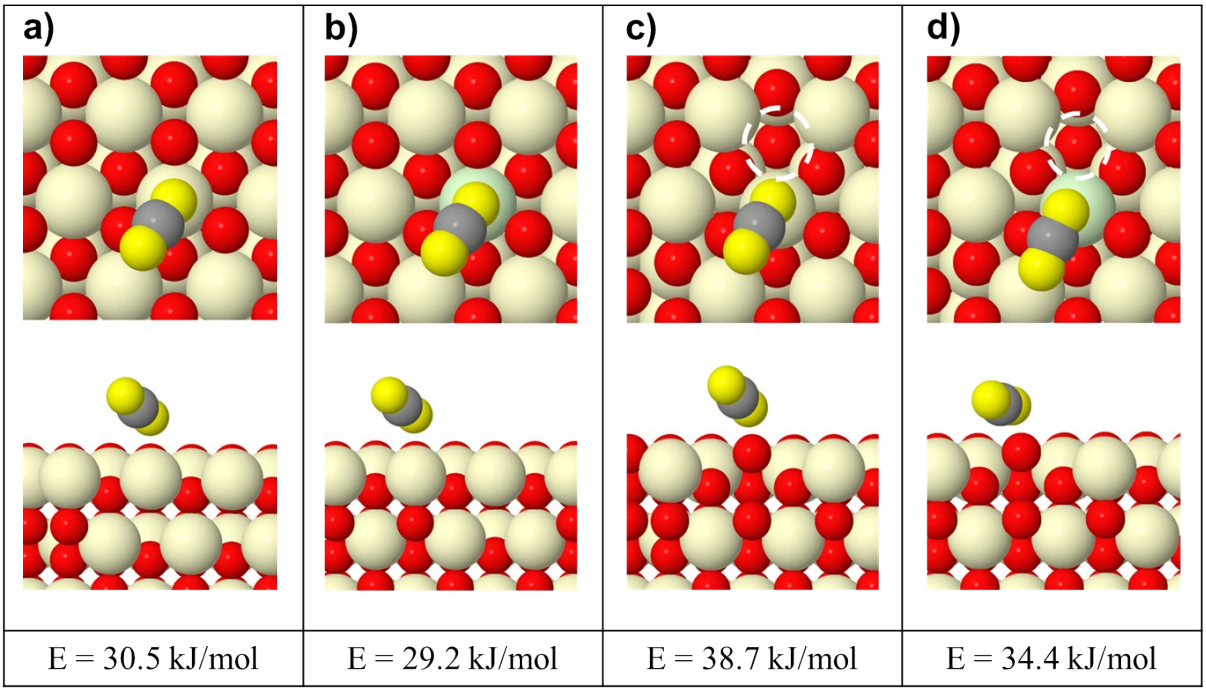

Fig. S16. DFT predicted favored configurations of CO_2 on **a)** CeO_2 (111) **b)** Pr-CeO_2 (111) surface **c)** O_V-CeO_2 (111) surface and, **d)** Pr&O_V-CeO_2 (111). The corresponding adsorption energies are provided the below figures. The oxygen atom bonding with carbon is colored yellow and the oxygen vacancy site is dashed and colored white.

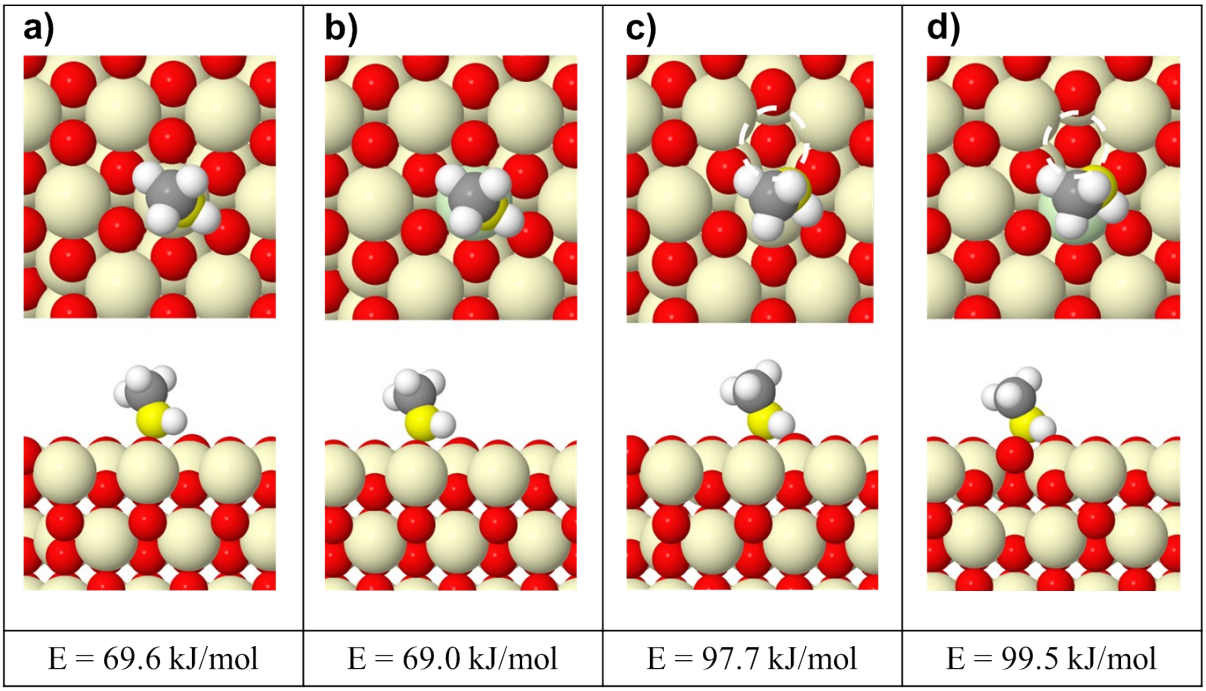

Fig. S17. DFT predicted favored configurations of CH_3OH on **a)** CeO_2 (111) **b)** Pr-CeO_2 (111) surface **c)** O_V-CeO_2 (111) surface and, **d)** Pr&O_V-CeO_2 (111). The corresponding adsorption energies are provided the below figures. The oxygen atom bonding with carbon is colored yellow and the oxygen vacancy site is dashed and colored white.

.

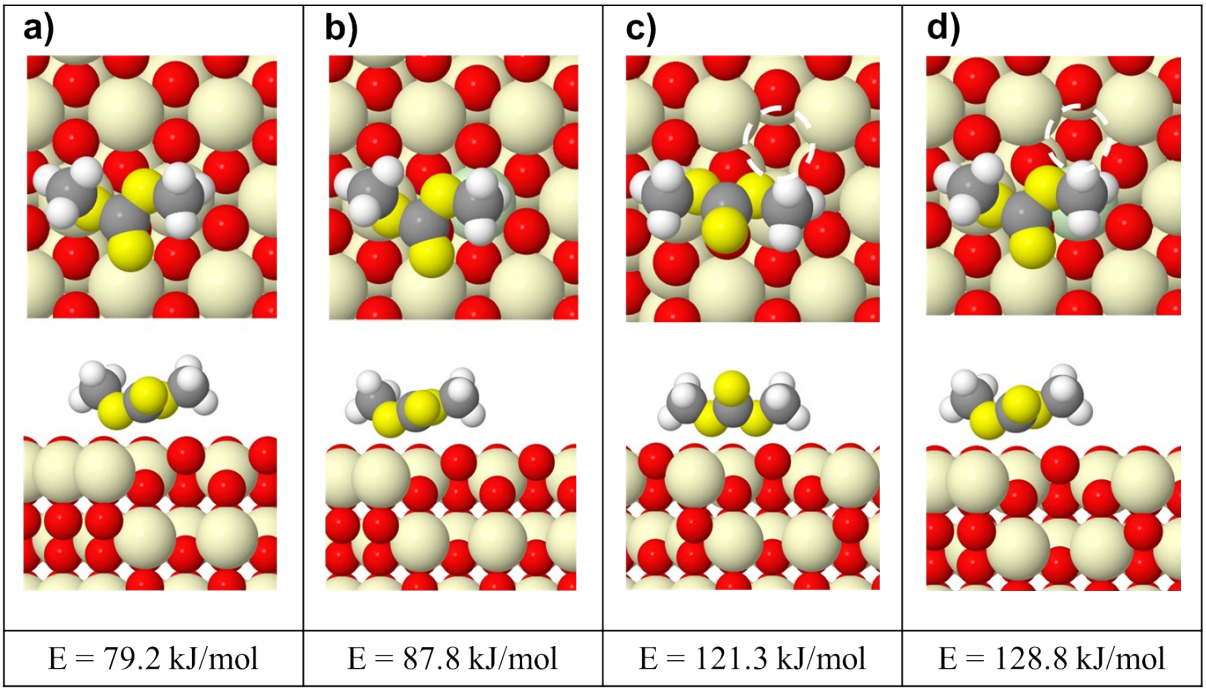

Fig. S18. DFT predicted favored configurations of DMC on **a)** CeO_2 (111) **b)** Pr-CeO_2 (111) surface **c)** O_V-CeO_2 (111) surface and, **d)** Pr&O_V-CeO_2 (111). The corresponding adsorption energies are provided the below figures. The oxygen atom bonding with carbon is colored yellow and the oxygen vacancy site is dashed and colored white.

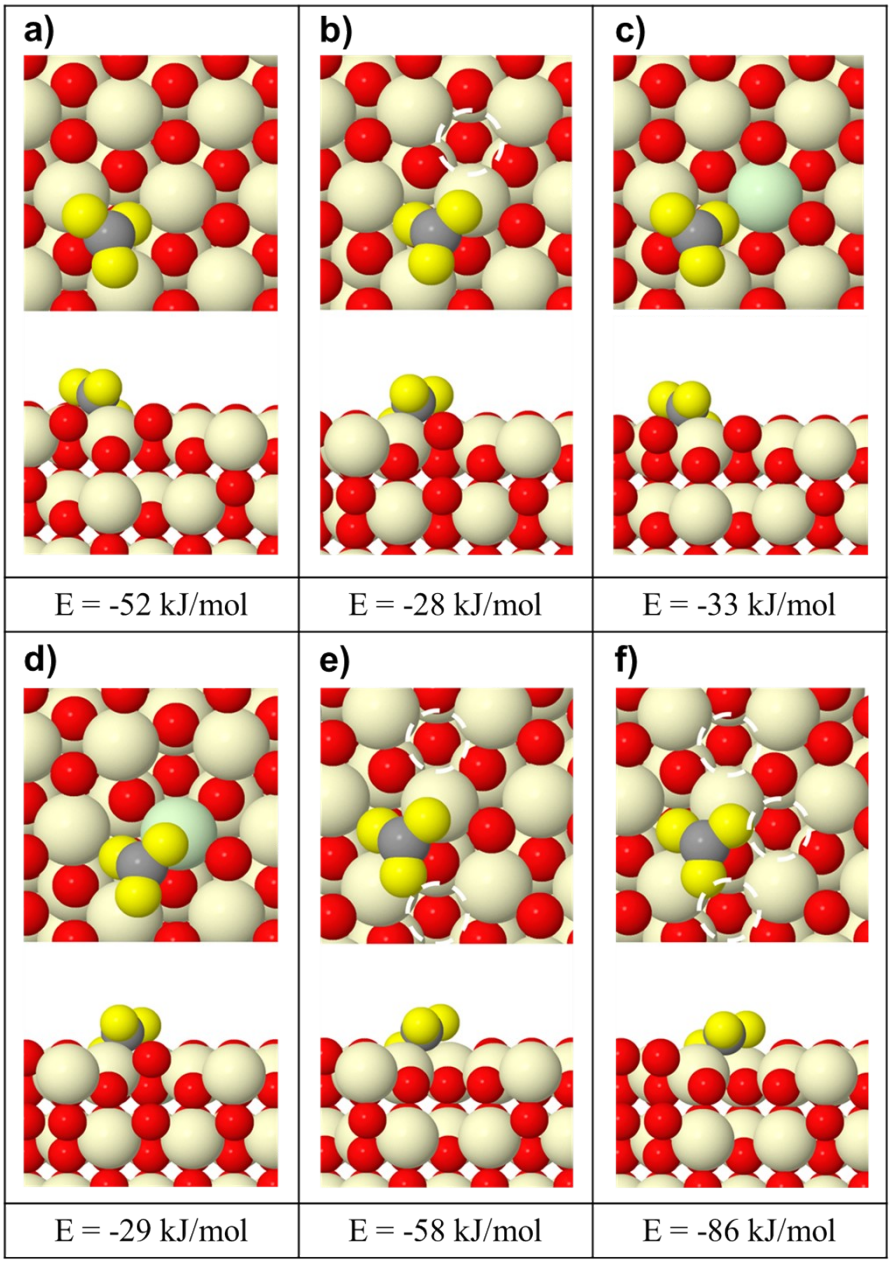

Fig. S19. ΔG of CO_2 activation on various CeO_2 (111) surface (a) pristine CeO_2, (b) CeO_2 w O_V, (c) Pr-CeO_2, (d) Pr-CeO_2 w O_V, (e) CeO_2 w $2O_V$ and (f) CeO_2 w $3O_V$. The oxygen atom bonding with carbon is colored yellow and the oxygen vacancy site is dashed and colored white.

Table S1. Weight percentages of Pr and Ce in a series of CePrOx catalysts determined by ICP-OES analysis

catalysts	Pr (wt.%)	Ce (wt.%)	Pr/(Ce+Pr)
CePr(7)Ox (BTC)	7.4	73.9	0.09
CePr(15)Ox (BTC)[a]	14.7	66.3	0.18
CePr(30)Ox (BTC)	29.8	57.8	0.34

[a]CePrOx (BTC) in main text corresponds to CePr(15)Ox (BTC)

Table S2. Results of XANES peak fitting using Ce L_{III} edge XANES spectra

Peak Position (eV)	CeO_2 (P)	CeO_2 (808)	CeO_2 (BTC)	CePrOx (BTC)	$Ce(NO_3)_3$
A: Pre-edge feature	5718.15	5718.24	5718.21	5718.17	-
B: Ce^{3+}, $2p \rightarrow 4f^1 5d^1$	5724.83	5724.53	5724.08	5724.58	5724.31
C: Ce^{4+},$2p \rightarrow 4f^0 5d^1$	5728.63	5728.82	5728.56	5728.57	-
D: Ce^{4+}, $2p \rightarrow 4f^1 5d^1 v$	5736.05	5736.07	5736.12	5736.04	-

Table S3. Peak position and full width at half maximum (FWHM) for the fitted 5 sets of spin-orbit split doublets of Ce 3d ($3d_{5/2}$ and $3d_{3/2}$) for CeO_2 (P)

Peak Assignment	Origin of cerium contribution	Peak decomposition	
		Peak	FWMH
v0	Ce^{3+}	880.2	1.04
u0	Ce^{3+}	898.4	1.04
v	Ce^{4+}	882.2	1.99
u	Ce^{4+}	900.7	1.99
v’	Ce^{3+}	884.2	2.85
u’	Ce^{3+}	902.9	2.85
v’’	Ce^{4+}	888.3	4.63
u’’	Ce^{4+}	907.1	4.63
v’’’	Ce^{4+}	898.1	2.14
u’’’	Ce^{4+}	916.5	2.14

Table S4. Peak position and full width at half maximum (FWHM) for the fitted 5 sets of spin-orbit split doublets of Ce 3d ($3d_{5/2}$ and $3d_{3/2}$) for CeO_2 (808)

Peak Assignment	Origin of cerium contribution	Peak decomposition	
		Peak	FWMH
v0	Ce^{3+}	880.1	1.60
u0	Ce^{3+}	898.5	1.60
v	Ce^{4+}	882.0	1.77
u	Ce^{4+}	900.5	1.77
v’	Ce^{3+}	884.4	3.0
u’	Ce^{3+}	902.9	3.0
v’’	Ce^{4+}	888.2	4.35
u’’	Ce^{4+}	906.7	3.14
v’’’	Ce^{4+}	897.9	1.98
u’’’	Ce^{4+}	916.2	1.87

Table S5. Peak position and full width at half maximum (FWHM) for the fitted 5 sets of spin-orbit split doublets of Ce 3d ($3d_{5/2}$ and $3d_{3/2}$) for CeO_2 (BTC)

Peak Assignment	Origin of cerium contribution	Peak decomposition	
		Peak	FWMH
v0	Ce^{3+}	880.2	1.35
u0	Ce^{3+}	898.5	1.35
v	Ce^{4+}	882.1	1.78
u	Ce^{4+}	900.6	1.78
v’	Ce^{3+}	884.4	3.8
u’	Ce^{3+}	902.7	3.8
v’’	Ce^{4+}	888.6	3.74
u’’	Ce^{4+}	907.1	3.74
v’’’	Ce^{4+}	898.0	2.09
u’’’	Ce^{4+}	916.4	2.09

Table S6. Peak position and full width at half maximum (FWHM) for the fitted 5 sets of spin-orbit split doublets of Ce 3d ($3d_{5/2}$ and $3d_{3/2}$) for CePrOx (BTC)

Peak Assignment	Origin of cerium contribution	Peak decomposition	
		Peak	FWMH
v0	Ce^{3+}	880.5	1.5
u0	Ce^{3+}	898.7	1.5
v	Ce^{4+}	882.0	1.9
u	Ce^{4+}	900.4	1.9
v’	Ce^{3+}	884.0	3.9
u’	Ce^{3+}	902.0	3.9
v’’	Ce^{4+}	888.4	3.5
u’’	Ce^{4+}	907.0	3.5
v’’’	Ce^{4+}	897.8	2.2
u’’’	Ce^{4+}	916.3	2.2

Table S7. Comparison of direct DMC formation rates from CO_2 and methanol over various catalysts

Catalysts	DMC Yield ($\mu mol_{DMC}/g_{cat} \cdot min$)	Reaction Conditions		Ref.
		Temperature	Pressure	
CePrOx (BTC)	5.1	120 °C	10 bar	This work
CePrOx (BTC)	3.2	120 °C	5 bar	This work
$Ce_{0.8}Zr_{0.2}O_2$	0.9	120 °C	18 bar	1
$Ti_{0.04}Ce0._{96}O_2$	4.5	140 °C	10 bar	2
CeO_2	1.8	140 °C	30 bar	3
Ce/SBA-15	0.6	130 °C	50 bar	4
$Y_{0.5}Fe_{0.5}O_x$	2.6	110 °C	80 bar	5
ZrO_2	2.2	160 °C	48 bar	6
$Fe_{0.7}Zr_{0.3}O_y$	1.8	140 °C	50 bar	7

References

1. H. J. Hofmann, A. Brandner and P. Claus, *Chemical Engineering & Technology*, 2012, **35**, 2140-2146.
2. Z. Fu, Y. Zhong, Y. Yu, L. Long, M. Xiao, D. Han, S. Wang and Y. Meng, *ACS Omega*, 2018, **3**, 198-207.
3. S. Rojas-Buzo, D. Salusso, A. Jouve, E. Bracciotti, M. Signorile and S. Bordiga, *Applied Catalysis B: Environment and Energy*, 2024, **346**, 123723.
4. Y. Pu, K. Xuan, F. Wang, A. Li, N. Zhao and F. Xiao, *RSC Advances*, 2018, **8**, 27216-27226.
5. W. Sun, L. Zheng, Y. Wang, W. Jia, W. Guo, Z. Liu, X. Ding, L. Wu and T. Fang, *Journal of CO_2 Utilization*, 2022, **58**, 101912.
6. T. Akune, Y. Morita, S. Shirakawa, K. Katagiri and K. Inumaru, *Langmuir*, 2018, **34**, 23-29.
7. A. Li, Y. Pu, F. Li, J. Luo, N. Zhao and F. Xiao, *Journal of CO_2 Utilization*, 2017, **19**, 33-39.